Article:
Sun, Y., Farnsworth, A., Joachimski, M.M. et al. (5 more authors) (2024) Mega El Niño instigated the end-Permian mass extinction. Science, 385 (6714). pp. 1189-1195. ISSN 0036-8075

https://doi.org/10.1126/science.ado2030

Title: Mega El Niño instigated the end-Permian mass extinction

Authors: Yadong Sun[1, 2]*†, Alexander Farnsworth[3,4]†, Michael M. Joachimski[2], Paul B. Wignall[5], Leopold Krystyn[6], David P.G. Bond[7], Domenico C.G. Ravidà[8], Paul J. Valdes[3,4]

Affiliations:

[1] State Key Laboratory of Biogeology and Environmental Geology, China University of Geosciences (Wuhan), Wuhan 430074, P.R. China

[2] GeoZentrum Nordbayern, Universität Erlangen-Nürnberg, Schlossgarten 5, 91054 Erlangen, Germany

[3] School of Geographical Sciences, University of Bristol, Bristol BS81SS, UK

[4] State Key Laboratory of Tibetan Plateau Earth System, Environment and Resources, Institute of Tibetan Plateau Research, Chinese Academy of Sciences, Beijing 100101, China

[5] School of Earth and Environment, University of Leeds, Leeds LS2 9JT, UK

[6] Department of Palaeontology, University of Vienna, Althanstrasse 14, A-1090 Wien, Austria

[7] School of Environmental Sciences, University of Hull, Hull, HU6 7RX, UK

[8] Department of Applied Geology, Georg-August-Universität Göttingen, Göttingen, Germany

*corresponding author E-mail: yadong.sun@cug.edu.cn

†These authors contributed equally to this work

Abstract: The ultimate driver of the end-Permian mass extinction is a topic of significant debate. Here, we use a multi-proxy and paleoclimate modelling approach to establish a unifying theory elucidating the heightened susceptibility of the Pangean world to prolonged and intensified El Niño events leading to an extinction state. As atmospheric pCO_2 doubled from ~410 to ~860 ppm in the latest Permian, the meridional overturning circulation collapsed, the Hadley cell contracted and El Niños intensified. The resultant deforestation, reef demise and plankton crisis marked the start of a cascading environmental disaster: reduced carbon sequestration initiated positive feedback, producing a warmer hothouse and, consequently, stronger El Niños. The compounding effects of elevated climate variability and mean state warming led to catastrophic but diachronous terrestrial and marine losses.

One-Sentence Summary:
The compounding effect of extreme El Niños and mean state warming led to catastrophic end-Permian losses.

Main Text:

The ultimate kill mechanism for the end-Permian mass extinction is uncertain. Rapid warming induced by eruptions of the voluminous Siberian Traps is regarded to have played a key role (*1*). However, over 20 volcanism-driven hyperthermals punctuate Phanerozoic history (*2*) and only a few coincide with extinctions, with none of them approaching the ~90% global species loss of the end-Permian (*3*). This raises the question of why the end-Permian world responded so strongly to CO_2-degassing and challenges our understanding of Earth system tipping points.

There is a clear mismatch in kill mechanisms and timing between marine and terrestrial losses during the end-Permian mass extinction (Fig. 1C). Equatorial sea surface temperature (SST) rose rapidly from ~26 °C to ~34 °C (*4*), likely exceeding the thermal tolerance of many marine organisms, particularly primary producers that underpin the marine food chain (*5*). However, many marine losses occurred ~17 kyr before substantial climate warming, suggesting that other kill mechanisms were at play: ocean deoxygenation is widely favored (*6*). However, in a setting characterized by atmospheric pO_2 levels higher than today (*7*), the impact of ocean anoxia on land would have been minimal. Even more puzzling, terrestrial extinctions, despite being diachronous themselves, began even earlier than the marine losses (*8, 9*), long before the potent warming. The loss of peatland (*10, 11*) and the replacement of gymnosperm forests by shrub-dominated terrestrial ecosystems (*12*) preceded the marine crisis by tens or even hundreds of thousands of years (*8*). Various causes have been proposed for the terrestrial crisis, including metal poisoning (*13*), intense UV-B radiation following ozone depletion (*14*) and acid rain (*15*). None of these alone can fully explain the scale, spatial heterogeneity, or the asynchronous nature of the end-Permian crisis.

Scant attention has been devoted to short-term climate oscillations occurring over interannual and interdecadal timescales in deep time, embedded within the context of longer-term climate change. Such modes of variability routinely induce large short-term fluctuations in temperature and the hydrological cycle through changes in weather patterns (*16*). We test the global climate system response to extreme greenhouse gas forcing in the Permian-Triassic (P-T) setting using paleotemperature proxy data to reconstruct the equatorial zonal SST gradient across the Tethys ocean (Fig. 1). Using a systematic combined approach incorporating proxy data, Earth system modelling (HadCM3BL) and sedimentary observations on a global scale, we establish a robust model for critical atmosphere-ocean coupling during the end-Permian catastrophe and propose a kill mechanism. We show that short-term climate fluctuations, which occur on annual time scales today, can be amplified by extreme greenhouse gas forcing, leading to a cascade of catastrophic terrestrial and marine losses.

Diminishing SST gradients

Zonal (east-west) and meridional (equator to mid-latitude) SST gradients regulate ocean-atmosphere feedback through Walker and Hadley circulations, and thus control low latitude climates. In modern oceans, a zonal SST gradient along the equator is prominent because equatorial easterlies push warm surface water to the west along both sides of the equator, generating a western warm pool. The westward movement of surface water also results in higher sea levels and a deeper thermocline in the western Pacific (*17*). Upwelling compensates for the loss of the warm surface layer in the east, generating cold tongues and a west-to-east tilted thermocline across the equatorial Pacific Ocean.

The P-T transition saw a dramatic decrease in the equatorial zonal SST gradient. Our paleotemperature dataset (*18*) shows that the late Permian equatorial zonal SST gradient within the Tethys was more prominent than that of modern Pacific. SSTs from westerly Cimmerian sites [e.g. Iran (*19*) and Armenia (*20*)] were consistently and considerably warmer than those from South China (*4*) in the east until 252.0 Ma. This zonal SST gradient decreased from >7–10°C in the late Permian, weakening to ~1–4°C across the P-T boundary, and was generally <4°C through the Early Triassic (Fig. 1B). The transition from high to low zonal SST gradients occurred abruptly within the latest Permian *Clarkina yini* conodont Zone (Fig. 1C).

Although less pronounced, our model simulations replicate these proxy data changes and additionally show an expanded equatorial warm pool and substantial thermocline deepening (Figs. S1 to S3). These profound changes in the ocean's thermal structure had substantial consequences for atmospheric circulation. Walker circulation weakened with the rising and sinking limbs both contracting to Panthalassa (Fig. 2). These changes coincide precisely with the decrease in the equatorial zonal SST gradient (Fig. 1C), leading to reduced horizontal and vertical moist advection. The ascending limb of the tropical Hadley circulation, already weaker than in the modern era, weakened further with warming, contracting in terms of both tropical overturning and convective potential (Figs. S4 and S5). Simultaneously, the descending limb widens at 500 hPa in the mid-latitudes, expanding arid regions poleward—a key feature of P-T sedimentary records (Fig. S6) and a climatic response predicted in future warming scenarios (*21*).

El Niño in a hothouse world

As the zonal SST changes are both the cause and consequence of Walker circulation fluctuations (*22*), flattened zonal SST gradients and weakened Walker circulation collectively imply a high probability of El Niños. Our proxy data showing diminished zonal SST gradients are mainly derived from the Tethys Ocean with further information coming from Panthalassa. They alone do not permit evaluation of the impact of El Niño Southern Oscillation (ENSO) due to its fine temporal scale, but we can address this in our Earth system modelling using the oceanic Niño index and by defining the Niño 3.4 (5°N–5°S, 120°–170°W) as equivalent to Panthalassa (Fig. 1A). We test this definition using empirical orthogonal function (EOF) analysis, which shows a strong 57.1% variance in the equivalent to the Niño 3.4 region of the Pacific, suggesting that Panthalassa's configuration is broadly similar to the modern Pacific. A series of pCO_2 sensitivity tests is carried out to understand the impact of warming on ENSO variability and its role in driving extinctions.

Model simulations show that SST anomalies in the Niño 3.4 equivalent region increase in both amplitude and longevity as atmospheric pCO_2 increases from 412 to 4000 ppm. Thus, the SST positive anomalies, marking El Niño conditions, increase from ~0.5–1.5°C in the Changhsingian prior to the main eruptions of Siberian Traps to ~4°C during maximum warmth in the Induan (Early Triassic), whilst their periodicity increases from 2–5 to 7–9 years (Fig. S7). These increases were accompanied by a disappearance of the El Niño-La Nina amplitude and evolution asymmetry (Fig. 3).

The disappearance of eastern cold tongues is a typical feature of El Niño conditions, but it is generally challenging to verify this with ancient proxy data. However, our conodont $\delta^{18}O$ values from the upper Smithian in Idaho (16.9 ‰) are comparable to contemporary $\delta^{18}O$ values from South China (16.8 ‰), Croatia (16.7 ‰), and Italy (16.5 ‰). Thus, the $\delta^{18}O$ difference, close to analytical reproducibility (±0.14 ‰, 1 σ), suggests that the Panthalassan "cold tongue" areas were

as warm as Tethys. These $\delta^{18}O$ values are comparable to those from Oman (16.3 ‰, ~20–30°S), suggesting there was an enormous warm pool across low latitude oceans, with SSTs reaching 39.4–41.9°C, and this extended to the extratropics during the hottest time of the Early Triassic. The warm "cold tongue" was accompanied by the cessation of denitrification on the eastern Panthalassan margin (*23*). The high SSTs of the late Smithian require atmospheric pCO_2 that was much greater than 4000 ppm to drive. However, our model simulations already show a steady deepening of the thermocline from ~30 m to over ~100 m across the P-T transition in eastern Panthalassa (Fig. S3). Together with weakened Walker circulation, this led to a reduction in equatorial upwelling. Collectively, proxy and modelling evidence suggests that the mean state warming in both Tethys and Panthalassa at the P-T boundary was probably El Niño-like.

Homogeneous SSTs along the equator weaken easterlies (both mean state and during El Niños) by reducing the east-west near-surface pressure gradient—a consistent feature of El Niños in the modern. Such changes link to sea level fluctuations that are also observed across the Tethys and Panthalassa oceans in the P-T time (*24*). There is no known evidence for ice coverage during the P-T interval and glacio-eustatic changes were insignificant. We suggest that regression recorded in some Tethyan sections in the west while transgressions featured along the eastern Panthalassan margin [e.g., western USA (*24, 25*)] was a function of strong ENSO impacting sedimentary records.

Was mega El Niño a permanent El Niño?

Whether climate warming has a significant impact on the strength and duration of El Niño is a matter of topical debate. Modern El Niños occur intermittently every two to seven years and typically last nine to 12 months but may have persisted for ~3 Myr in the Pliocene (*26*). Many features of future El Niños simulated by CMIP6 models remain uncertain, but stronger El Niños with fast onset and slow decay will likely occur (*27*).

Our simulations suggest that as the world warmed across the P-T boundary both the magnitude and duration of El Niño increased but this was not accompanied by the establishment of a permanent El Niño (Fig. 3). Our proxy-derived zonal SST gradients across the equatorial Tethys show consistently high values in the Permian and consistently low values in the Early Triassic (Fig. 1, B and C). This should not be interpreted as an establishment of permanent El Niño but is a function of the time-averaged homogenization of paleotemperatures in "bulk" samples. Each data point was measured from ~50 conodonts from a sub-10–100 kyr interval thereby averaging any short-term anomaly. Our data collectively indicate that the Permian was largely dominated by neutral ENSO states, whilst El Niños became prominent shortly before the P-T boundary, to an extent that influenced the long-term climate proxy record in the Tethys (Fig. 1B), but did not diminish the simulated zonal SST anomalies in the Panthalassa (Fig. 3; *18*).

Climate States

The transition to conditions with prolonged, episodic mega-ENSO events created a world of exceptional climate variability (Fig. 3), with intra-annual variability controlled by the large land-ocean thermal contrast of Pangea (*28*), and annual to decadal variability controlled by ENSO, whilst millennial variability was controlled by pCO_2 and possibly orbital forcing. The net result was a broadly hot but extraordinarily unstable and variable climate (Fig. 4, and Figs. S8, S9, S11 to S14).

On land, low and mid-latitude climates became nearly unified across the P-T boundary, leading to a remarkable transition from regionally-diverse sedimentary facies to higher-energy fluvial sedimentation style, frequently represented by braided river facies assemblages (Fig. S6). This shift signals the onset of a more unstable climate state, characterized by moisture deficits and irregular rainfall, coupled with generally greater surface runoff and temperature extremes (*18*). Such conditions, presumably driven by both Pangean monsoon and ENSO cycles, occurred poleward and equatorward from ~10° to ~60° in both hemispheres but are less apparent in high-latitudes (*29*), probably because ENSO is primarily a low-latitude climate anomaly (Fig. 4; Fig. S9).

Unlike other hothouse intervals such as the middle Cretaceous (*30*), in the P-T case, the ascending limb of the Hadley cells weakened and contracted while the descending limb expanded further towards the poles (Figs. S4, S5). This is clearly manifested in the Turpan-Kumul Basin (Xinjiang, NW China), where plant-bearing Upper Permian fluvial-lacustrine and deltaic depositional systems are abruptly overlain by Lower Triassic drylands, suggesting a sudden shift in climate regime at ~44°N (Fig. S6A). These areas were probably as dry as modern subtropical deserts, but with pronounced seasonal torrential rains, indicated by the common occurrence of sheet-like sandstones and pebbly deposits produced by flash flooding and ephemeral rivers (Fig. S6, B to D). The transition to higher-energy fluvial systems across the P-T boundary has been previously attributed to reduced bank stability from plant die-off (*31*), but this also occurs in extremely arid settings where pre-crisis vegetation was already minimal or absent (*32*). We propose that the shift to a much more irregular precipitation regime was the main driver of the P-T sedimentary evolution on land.

Stronger El Niños and warmer hothouse

The decrease in the zonal SST gradient at the end of the Permian during an El Niño likely caused two inter-connected positive feedbacks through interplays with the Walker circulation. Weakened easterlies led to the eastward retreat of warm waters, deepening the thermocline in the east (Fig. S3), which in turn further enhanced El Niño conditions (Bjerknes feedback, *17, 22*). The development of increasingly stronger El Niños is simultaneously coupled with changes in the low latitude hydrological cycle. Warm waters generate high, rain-bearing convective clouds that are less reflective than low, non-rain-bearing stratus clouds that follow cooler waters. Thus, El Niño redistributes low latitude precipitation as the warm pool expands eastward (*33*). Decreases in low latitude coverage by stratus clouds would also reduce the overall planetary albedo, exacerbating hothouse conditions.

Impact on the terrestrial realm

The synergy of stronger ENSO and a warm climate generates an oscillating dry-wet contrast over land and amplifies the unevenness of precipitation on a global scale (Fig. 4). During El Niños, the heat stored in the ocean is released into the atmosphere, leading to severe drought and extreme heat. Today, these conditions have destabilized tropical forests, causing Amazonian and African rainforest dieback (*34, 35*). In the P-T time, our composite analysis of five consecutive ENSO intervals reveals large climate anomalies compared to the background state. These include a strong, high-temperature land-ocean teleconnection in the tropics and extratropics, mildly cooler high latitudes, and a re-distribution of low latitude precipitation predominantly over Panthalassa

and around the Tethys margins during El Niños (Fig. 4). Roughly opposite trends occur during La Ninas (Fig. S9). Geologic evidence for these changes includes the widespread development of fluvial facies produced by irregular runoff and flashy discharge in the Early Triassic (Figs. S6, S10), indicating an unprecedented homogeneity of low latitude climates that featured highly variable dry and wet seasons (Figs. S11to S14).

As the duration of El Niños extended from months to years (Fig. 3), prolonged warmth and drought in vast areas of Pangea would have stressed plants further amidst background warming and an increased frequency of wildfires. This is evidenced by the zenith of charcoal deposition in equatorial peatlands as the climate regime transitioned from humid to semi-arid (*11*). Wet periods created substantial fuel reserves and were followed by long-lasting droughts with accompanying heat that resulted in severe wildfires. This drove the eventual extinction of rainforest plants and, consecutively, the collapse of the charcoal "spike" (Fig. 1C), reflecting the loss of terrestrial biomass and fuel for fire. As warming and aridity intensified, vegetation was increasingly subject to fire susceptibility (Fig. S15), compromising carbon sequestration in the terrestrial realm (*10*) and elevating atmospheric pCO_2 further.

Frequent droughts force physiological changes in plants and favor short-lived taxa capable of thriving in sporadic wet intervals whilst enduring prolonged dry spells in their seed or spore stage. This is reflected by a floral shift in preference across the P-T crisis towards lightly-built shrubs rather than trees, as indicated by the post-extinction prevalence of the isoetalean lycopsids *Pleuromeia* and *Annalepis*, in contrast to the gymnosperm-dominated forests of the Permian (*36*). A similar adaptation to life cycles exploiting brief wet intervals probably explains the selective survival of insect groups. Their fossil record, although patchy, reveals significant declines in most groups, closely linked to the loss of habitats and food plants (*37*) during deforestation (Fig. S16). However, those with aquatic larval stages (e.g., amongst palaeopteran families) fared better than those with an entirely terrestrial life cycle (*37*), indicating an ability to exploit the wet intervals. Early Triassic assemblages were dominated by beetles, cockroaches and mayflies (*37, 38*). However, the post-extinction climatic conditions were overall harsh (Fig. S8; *39*), with none of the major insect groups showing opportunistic radiation (*37*).

The extreme effects of ENSO were most clearly manifest in low latitude ocean-atmosphere interactions, but their consequences were global (Fig. 4) and ensured that the modest changes in mean background conditions were greatly amplified (Fig. 5). The most prominent change in the P-T terrestrial realm was the dramatic deforestation in both hemispheres in response to the initial pCO_2 doubling. Our simulations indicate that the southern deciduous taiga was impacted first. It retreated poleward in Gondwana and decreased by 46.6% in coverage (equivalent to ~ 21×10^6 km^2 forest loss) within ~25 kyr (Fig. S16). This was followed by successive deforestation in northern mid-latitudes and tropics (Fig. S16), a pattern confirmed by the fossil record of the regions (*8, 9, 40*). However, what drove the earlier deforestation in southern high latitudes is unexplained. The disappearance of the Permian *Glossopteris* flora in the Sydney Basin (70°S) occurred ~380 kyr (*8*) before the rise in equatorial SSTs. Our simulations indicate the region was particularly vulnerable to ENSO impact, much like Australia today (Fig. 4 and Fig. S9). Specifically, warmer and dryer summers were prominent during El Niños (Fig. S14), aligning with sedimentological evidence for increasingly prolonged droughts at the level directly above the last Permian flora (*29*).

Impact on the marine realm

Most phytoplankton and zooplankton have a thermal tolerance up to ~35°C, but the optimal temperature range for vital processes (e.g. reproduction) is often narrower than the range required for survival (*5*), particularly in species with lifespans shorter than a year. Consequently, marine plankton are particularly susceptible to inter-annual climate perturbations. Their decline can trigger bottom-up trophic cascades, as seen during recent marine heat waves (*41*). The P-T transition witnessed a turnover in the composition of primary producers, whereby the dominant eukaryotic plankton groups became extinct and were replaced by bacteria (including cyanobacteria), acritarchs and prasinophytes (*42*). The changes amongst plankton groups are also faithfully documented by a crisis amongst radiolarians (*43*), a heterotrophic group with siliceous skeletons that have a good fossil record. They suffered major losses ~40 kyrs prior to the main marine losses, coincident with the onset of enhanced El Niños (Fig. 1C) indicating that planktonic communities were the first to be stressed by augmented interannual variability and climatic extremes (Fig. 1C).

Reefs are amongst the most vulnerable components of marine ecosystems. Both coral and non-coral reefs have suffered mass mortality in recent marine heat waves (*5*), underscoring their limited capacity to withstand rapid SST increases. The end-Permian crisis saw not only the extinction of all Paleozoic corals but the demise of metazoan reefs of all types (*44*), leading to one of the Phanerozoic's most prominent reef gaps (*45*). The last Permian reefs persisted to a level correlative with the top of Meishan stratotype Bed 23 (*44, 46*). Thus, their demise coincided with the advent of intensified El Niños and the weakening of global Meridional Ocean Circulation (MOC; Fig. 1C and Fig. S17), heralding the severe losses to come.

The main marine mass extinction coincides with the onset of widespread ocean anoxia and postdates the start of a major negative carbon isotope excursion (Fig. 1). Anoxia occurred during a phase of rapid ocean warming, increasing stratification and reorganization of the global MOC, which was likely a consequence of these changes (Figs. S1 to S3 and S17). The MOC collapsed from its robust pre-crisis state, featuring a strong, well-mixed cell with mid- and deepwater overturning in the northern hemisphere, to a shallower northward cell as pCO_2 doubled from 412 ppm to 857 ppm (Fig. S17). The proxy-recorded onset of ocean anoxia at Meishan (*47*) is attributed to a global expansion of anoxic water masses, and lagged the collapse of the MOC by ~3–5 kyr—a brief interval comparable to the residence time of seawater. The MOC mixing cells weakened and shallowed further with increasing pCO_2 (Fig. S17), suggesting the pre-crisis P-T world was already highly sensitive to small changes in pCO_2.

An El Niño-instigated extinction

The shift to a new climate state with enhanced variability at the end of the Permian was likely rapid. Employing a Bayesian age model grounded in U-Pb dating (*48*), the transition is estimated to have occurred within ~5 ± 3 kyr, predating the onset of marine extinction by ~40±30 kyr. This coincided with the onset of a protracted decrease in $\delta^{13}C$ and a minor, ~4°C increase in equatorial SST (Fig. 1C). Because Upper Permian marine faunas maintained their diversity, it is generally thought that there were no environmental perturbations at this time. However, two-thirds of the volume of Siberian Traps lava and pyroclastic eruptions occurred pre-extinction (*1*), and our study shows that they coincide with progressively enhanced ENSO activity (Figs. 1 and 3). The

initiation of a major crisis, encompassing deforestation on land (*8*), the collapse of MOC, extinctions in marine plankton, and the demise of reefs, all occurred during the initial pCO_2 doubling to 857 ppm and coincided with a decrease in the equatorial zonal SST gradient in Tethys (Fig. 1 and Figs. S16, S17). Thus, in the P-T world, even relatively small greenhouse gas emissions and warming were sufficient to tip the climate into a state characterized by prolonged and intense El Niño phases. This introduced extremes in low latitude temperature and precipitation that stressed terrestrial ecosystems (Figs. 4 and 5). Drought intervals were too prolonged for trees to survive, strongly favoring opportunists amongst both plants and insects that were able to complete their life cycle during wet periods. In the ocean, planktonic groups, with their sub-annual lifecycles, were also severely impacted, but the resilience of the marine biosphere ensured its survival until it succumbed to progressive warming and ocean de-oxygenation. The losses in biomass, in turn, reduced carbon sequestration, creating a warmer hothouse with stronger El Niños.

Conclusions

El Niño events today are known to cause coral bleaching (*5*), the mass mortality of fish and birds (*49*), and they have profound impacts on human society. However, the ecological impact and future trajectory of extreme El Niños against a backdrop of global warming is not yet known. The Pangean supercontinent paleogeography was seemingly more susceptible to ever-increasing ENSO events with increasing pCO_2. The end-Permian crisis reveals that intensified ENSO increases the risk of extinction, enhancing low latitude warmth that in turn created stronger El Niños. For terrestrial communities, prolonged extremes (droughts and high temperatures) led to extinctions, whilst the oceans suffered from heat stress and the expansion of anoxia, with equally disastrous consequences for life. Because the oceans warm more slowly than land and marine organisms have higher motility (actively or passively), terrestrial ecosystems are more vulnerable to extinction threats during intensified El Niños. Consequently, the P-T transition saw the marine extinction lag by ~40±30 thousand years, a short interval geologically, and one that is alarmingly, on human timescales, as we move towards an ever more variable climate regime.

References and Notes

1. S. D. Burgess, S. A. Bowring, High-precision geochronology confirms voluminous magmatism before, during, and after Earth's most severe extinction. *Science Advances* **1**, e1500470 (2015).
2. C. R. Scotese, H. Song, B. J. W. Mills, D. G. van der Meer, Phanerozoic paleotemperatures: The earth's changing climate during the last 540 million years. *Earth-Science Reviews* **215**, 103503 (2021).
3. J.-x. Fan *et al.*, A high-resolution summary of Cambrian to Early Triassic marine invertebrate biodiversity. *Science* **367**, 272-277 (2020).
4. M. M. Joachimski *et al.*, Climate warming in the latest Permian and the Permian-Triassic mass extinction. *Geology* **40**, 195-198 (2012).
5. K. E. Smith *et al.*, Biological Impacts of Marine Heatwaves. *Annual Review of Marine Science* **15**, 119-145 (2023).
6. P. B. Wignall, R. J. Twitchett, Oceanic Anoxia and the End Permian Mass Extinction. *Science* **272**, 1155-1158 (1996).

7. B. J. W. Mills, A. J. Krause, I. Jarvis, B. D. Cramer, Evolution of Atmospheric O2 Through the Phanerozoic, Revisited. *Annual Review of Earth and Planetary Sciences* **51**, 253-276 (2023).
8. C. R. Fielding *et al.*, Age and pattern of the southern high-latitude continental end-Permian extinction constrained by multiproxy analysis. *Nature Communications* **10**, 385 (2019).
9. R. A. Gastaldo *et al.*, The base of the Lystrosaurus Assemblage Zone, Karoo Basin, predates the end-Permian marine extinction. *Nature Communications* **11**, 1428 (2020).
10. G. J. Retallack, J. J. Veevers, R. Morante, Global coal gap between Permian-Triassic extinction and Middle Triassic recovery of peat-forming plants. *Geological Society of America Bulletin* **108**, 195-207 (1996).
11. D. Chu *et al.*, Ecological disturbance in tropical peatlands prior to marine Permian-Triassic mass extinction. *Geology*, (2020).
12. C. V. Looy, W. A. Brugman, D. L. Dilcher, H. Visscher, The delayed resurgence of equatorial forests after the Permian–Triassic ecologic crisis. *Proceedings of the National Academy of Sciences of the United States of America* **96**, 13857-13862 (1999).
13. D. Chu *et al.*, Metal-induced stress in survivor plants following the end-Permian collapse of land ecosystems. *Geology*, (2021).
14. F. Liu *et al.*, Dying in the Sun: Direct evidence for elevated UV-B radiation at the end-Permian mass extinction. *Science Advances* **9**, eabo6102 (2023).
15. B. A. Black, J.-F. Lamarque, C. A. Shields, L. T. Elkins-Tanton, J. T. Kiehl, Acid rain and ozone depletion from pulsed Siberian Traps magmatism. *Geology* **42**, 67-70 (2014).
16. M. R. Allen, W. J. Ingram, Constraints on future changes in climate and the hydrologic cycle. *Nature* **419**, 224-232 (2002).
17. M. Latif, N. S. Keenlyside, El Niño/Southern Oscillation response to global warming. *Proceedings of the National Academy of Sciences* **106**, 20578-20583 (2009).
18. See supplementary materials.
19. M. Schobben, M. M. Joachimski, D. Korn, L. Leda, C. Korte, Palaeotethys seawater temperature rise and an intensified hydrological cycle following the end-Permian mass extinction. *Gondwana Research* **26**, 675-683 (2014).
20. M. M. Joachimski, A. S. Alekseev, A. Grigoryan, Y. A. Gatovsky, Siberian Trap volcanism, global warming and the Permian-Triassic mass extinction: New insights from Armenian Permian-Triassic sections. *GSA Bulletin* **132**, 427-443 (2020).
21. B. I. Cook *et al.*, Twenty-first century drought projections in the CMIP6 forcing scenarios. *Earth's Future* **8**, e2019EF001461 (2020).
22. A. V. Fedorov, S. G. Philander, Is El Niño changing? *Science* **288**, 1997-2002 (2000).
23. S. D. Schoepfer, C. M. Henderson, G. H. Garrison, P. D. Ward, Cessation of a productive coastal upwelling system in the Panthalassic Ocean at the Permian–Triassic boundary. *Palaeogeography, Palaeoclimatology, Palaeoecology* **313-314**, 181-188 (2012).
24. P. B. Wignall, A. Hallam, Anoxia as a cause of the Permian/Triassic mass extinction: facies evidence from northern Italy and the western United States. *Palaeogeography, Palaeoclimatology, Palaeoecology* **93**, 21-46 (1992).
25. B. Kummel, Paleoecology of Lower Triassic formations of southeastern Idaho and adjacent areas. *Geological Society of America Memoirs* **67**, 437-468 (1957).
26. M. W. Wara, A. C. Ravelo, M. L. Delaney, Permanent El Niño-like conditions during the Pliocene warm period. *Science* **309**, 758-761 (2005).
27. H. Lopez, S.-K. Lee, D. Kim, A. T. Wittenberg, S.-W. Yeh, Projections of faster onset and slower decay of El Niño in the 21st century. *Nature Communications* **13**, 1915 (2022).

28. Y. Hu *et al.*, Emergence of the modern global monsoon from the Pangaea megamonsoon set by palaeogeography. *Nature Geoscience*, (2023).
29. C. R. Fielding *et al.*, Sedimentology of the continental end-Permian extinction event in the Sydney Basin, eastern Australia. *Sedimentology* **68**, 30-62 (2021).
30. H. Hasegawa *et al.*, Drastic shrinking of the Hadley circulation during the mid-Cretaceous Supergreenhouse. *Climate of the Past* **8**, 1323-1337 (2012).
31. P. D. Ward, D. R. Montgomery, R. Smith, Altered river morphology in South Africa related to the Permian-Triassic extinction. *Science* **289**, 1740-1743 (2000).
32. C. M. S. Scherer *et al.*, The stratigraphic puzzle of the permo-mesozoic southwestern Gondwana: The Paraná Basin record in geotectonic and palaeoclimatic context. *Earth-Science Reviews* **240**, 104397 (2023).
33. G. A. Vecchi, A. T. Wittenberg, El Niño and our future climate: where do we stand? *WIREs Climate Change* **1**, 260-270 (2010).
34. J. C. Jiménez-Muñoz *et al.*, Record-breaking warming and extreme drought in the Amazon rainforest during the course of El Niño 2015–2016. *Scientific Reports* **6**, 33130 (2016).
35. J.-P. Wigneron *et al.*, Tropical forests did not recover from the strong 2015–2016 El Niño event. *Science Advances* **6**, eaay4603 (2020).
36. S. F. Greb, W. A. DiMichele, R. A. Gastaldo, in *Wetlands Through Time. Geological Society of America Special Paper 399,* S. F. Greb, W. A. DiMichele, Eds. (Geological Society of America, Boulder, CO, 2006), pp. 1-40.
37. C. Jouault, A. Nel, V. Perrichot, F. Legendre, F. L. Condamine, Multiple drivers and lineage-specific insect extinctions during the Permo–Triassic. *Nature Communications* **13**, 7512 (2022).
38. D. E. Shcherbakov, Madygen, Triassic Lagerstätte number one, before and after Sharov. *Alavesia* **2**, 113-124 (2008).
39. Y. D. Sun *et al.*, Lethally hot temperatures during the Early Triassic greenhouse. *Science* **338**, 366-370 (2012).
40. W. Guo *et al.*, Late Permian–Middle Triassic magnetostratigraphy in North China and its implications for terrestrial-marine correlations. *Earth and Planetary Science Letters* **585**, 117519 (2022).
41. L. A. Arteaga, C. S. Rousseaux, Impact of Pacific Ocean heatwaves on phytoplankton community composition. *Communications Biology* **6**, 263 (2023).
42. C. Cao *et al.*, Biogeochemical evidence for euxinic oceans and ecological disturbance presaging the end-Permian mass extinction event. *Earth and Planetary Science Letters* **281**, 188-201 (2009).
43. Q. Feng *et al.*, Radiolarian evolution during the latest Permian in South China. *Global and Planetary Change* **55**, 177-192 (2007).
44. R. C. Martindale, W. J. Foster, F. Velledits, The survival, recovery, and diversification of metazoan reef ecosystems following the end-Permian mass extinction event. *Palaeogeography, Palaeoclimatology, Palaeoecology* **513**, 100-115 (2019).
45. W. Kiessling, Geologic and biologic controls on the evolution of reefs. *Annual Review of Ecology, Evolution, and Systematics* **40**, 173-192 (2009).
46. X. Li *et al.*, Factors controlling carbonate platform asymmetry: Preliminary results from the Great Bank of Guizhou, an isolated Permian–Triassic Platform in the Nanpanjiang Basin, south China. *Palaeogeography, Palaeoclimatology, Palaeoecology* **315-316**, 158-171 (2012).
47. L. Xiang *et al.*, Oceanic redox evolution around the end-Permian mass extinction at Meishan, South China. *Palaeogeography, Palaeoclimatology, Palaeoecology* **544**, 109626 (2020).

48. S. D. Burgess, S. Bowring, S.-z. Shen, High-precision timeline for Earth's most severe extinction. *Proceedings of the National Academy of Sciences* **111**, 3316-3321 (2014).
49. R. T. Barber, F. P. Chavez, Biological Consequences of El Niño. *Science* **222**, 1203-1210 (1983).
50. S. Xie *et al.*, Changes in the global carbon cycle occurred as two episodes during the Permian Triassic crisis. *Geology* **35**, 1083-1086 (2007).
51. S.-z. Shen *et al.*, High-resolution $\delta^{13}C_{carb}$ chemostratigraphy from latest Guadalupian through earliest Triassic in South China and Iran. *Earth and Planetary Science Letters* **375**, 156-165 (2013).
52. S. E. Grasby *et al.*, Isotopic signatures of mercury contamination in latest Permian oceans. *Geology* **45**, 55-58 (2017).
53. M. M. Joachimski *et al.*, Five million years of high atmospheric CO_2 in the aftermath of the Permian-Triassic mass extinction. *Geology* **50**, 650-654 (2022).
54. J. Wu *et al.*, Stepwise deforestation during the Permian-Triassic boundary crisis linked to rising temperatures. *Earth and Planetary Science Letters* **620**, 118350 (2023).
55. F. Yang *et al.*, Collapse of Late Permian chert factories in equatorial Tethys and the nature of the Early Triassic chert gap. *Earth and Planetary Science Letters* **600**, 117861 (2022).
56. M. M. Joachimski *et al.*, Devonian climate and reef evolution: Insights from oxygen isotopes in apatite. *Earth and Planetary Science Letters* **284**, 599-609 (2009).
57. E. Pucéat *et al.*, Revised phosphate-water fractionation equation reassessing paleotemperatures derived from biogenic apatite. *Earth and Planetary Science Letters* **298**, 135-142 (2010).
58. S.-z. Shen *et al.*, Calibrating the End-Permian Mass Extinction. *Science* **334**, 1367-1372 (2011).
59. J. Haslett, A. Parnell, A simple monotone process with application to radiocarbon-dated depth chronologies. *Journal of the Royal Statistical Society: Series C (Applied Statistics)* **57**, 399-418 (2008).
60. C.-q. Cao, Q.-f. Zheng, High-resolution lithostratigraphy of the Changhsingian Stage in Meishan section D, Zhejiang. *Journal of Stratigraphy* **31**, 14-22 (2007).
61. S. N. Wood, Fast stable restricted maximum likelihood and marginal likelihood estimation of semiparametric generalized linear models. *Journal of the Royal Statistical Society: Series B (Statistical Methodology)* **73**, 3-36 (2011).
62. P. J. Valdes *et al.*, The BRIDGE HadCM3 family of climate models: HadCM3@Bristol v1.0. *Geoscientific Model Development* **10**, 3715-3743 (2017).
63. P. J. Valdes, C. R. Scotese, D. J. Lunt, Deep ocean temperatures through time. *Climate of the Past* **17**, 1483-1506 (2021).
64. A. Farnsworth *et al.*, Past East Asian monsoon evolution controlled by paleogeography, not CO_2. *Science Advances* **5**, eaax1697 (2019).
65. L. A. Jones, P. D. Mannion, A. Farnsworth, F. Bragg, D. J. Lunt, Climatic and tectonic drivers shaped the tropical distribution of coral reefs. *Nature Communications* **13**, 3120 (2022).
66. P. M. Cox *et al.*, The impact of new land surface physics on the GCM simulation of climate and climate sensitivity. *Climate Dynamics* **15**, 183-203 (1999).
67. J. T. Kiehl, C. A. Shields, Sensitivity of the Palaeocene–Eocene Thermal Maximum climate to cloud properties. *Philosophical Transactions of the Royal Society A: Mathematical, Physical and Engineering Sciences* **371**, 20130093 (2013).
68. N. Sagoo, P. Valdes, R. Flecker, L. J. Gregoire, The Early Eocene equable climate problem: can perturbations of climate model parameters identify possible solutions? *Philosophical*

Transactions of the Royal Society A: Mathematical, Physical and Engineering Sciences **371**, 20130123 (2013).
69. M. D. Cox, A primitive equation, 3-dimensional model of the ocean. *GFDL ocean group technical report* **1**, (1984).
70. M. Collins, S. F. B. Tett, C. Cooper, The internal climate variability of HadCM3, a version of the Hadley Centre coupled model without flux adjustments. *Climate Dynamics* **17**, 61-81 (2001).
71. A. Farnsworth *et al.*, Climate sensitivity on geological timescales controlled by nonlinear feedbacks and ocean circulation. *Geophysical Research Letters* **46**, 9880-9889 (2019).
72. R. Joseph, S. Nigam, ENSO evolution and teleconnections in IPCC's twentieth-century climate simulations: Realistic representation? *Journal of Climate* **19**, 4360-4377 (2006).
73. G. L. Foster, D. L. Royer, D. J. Lunt, Future climate forcing potentially without precedent in the last 420 million years. *Nature Communications* **8**, 14845 (2017).
74. D. Gough, in *Physics of Solar Variations: Proceedings of the 14th ESLAB Symposium held in Scheveningen, The Netherlands, 16–19 September, 1980*. (Springer, 1981), pp. 21-34.
75. J. O. Kaplan *et al.*, Climate change and Arctic ecosystems: 2. Modeling, paleodata-model comparisons, and future projections. *Journal of Geophysical Research: Atmospheres* **108**, (2003).
76. C. J. R. Williams *et al.*, African Hydroclimate During the Early Eocene From the DeepMIP Simulations. *Paleoceanography and Paleoclimatology* **37**, e2022PA004419 (2022).
77. S.-F. Li *et al.*, Orographic evolution of northern Tibet shaped vegetation and plant diversity in eastern Asia. *Science Advances* **7**, eabc7741.
78. J. L. Brown, D. J. Hill, A. M. Dolan, A. C. Carnaval, A. M. Haywood, PaleoClim, high spatial resolution paleoclimate surfaces for global land areas. *Scientific Data* **5**, 180254 (2018).
79. A. Farnsworth *et al.*, Paleoclimate model-derived thermal lapse rates: Towards increasing precision in paleoaltimetry studies. *Earth and Planetary Science Letters* **564**, 116903 (2021).
80. J. N. Bahcall, M. H. Pinsonneault, S. Basu, Solar Models: Current Epoch and Time Dependences, Neutrinos, and Helioseismological Properties. *The Astrophysical Journal* **555**, 990 (2001).
81. N. Preto, E. Kustatscher, P. B. Wignall, Triassic climates—State of the art and perspectives. *Palaeogeography, Palaeoclimatology, Palaeoecology* **290**, 1-10 (2010).
82. E. Hawkins, R. Sutton, The potential to narrow uncertainty in regional climate predictions. *Bulletin of the American Meteorological Society* **90**, 1095-1108 (2009).
83. H. Zhang *et al.*, The terrestrial end-Permian mass extinction in South China. *Palaeogeography, Palaeoclimatology, Palaeoecology* **448**, 108-124 (2016).
84. K. Jewuła, W. Trela, A. Fijałkowska-Mader, Sedimentary and pedogenic record of seasonal humidity during the Permian-Triassic transition on the SE margin of Central European Basin (Holy Cross Mountains, Poland). *Palaeogeography, Palaeoclimatology, Palaeoecology* **564**, 110154 (2021).
85. D. C. G. Ravidà, L. Caracciolo, S. Henares, M. Janssen, H. Stollhofen, Drainage and environmental evolution across the Permo-Triassic boundary in the south-east Germanic Basin (north-east Bavaria). *Sedimentology* **69**, 501-536 (2022).
86. M. Hiete, H.-G. Röhling, C. Heunisch, U. Berner, Facies and climate changes across the Permian–Triassic boundary in the North German Basin: insights from a high-resolution organic carbon isotope record. *Geological Society, London, Special Publications* **376**, 549-574 (2013).

87. F. Käsbohrer, J. Kuss, Lower Triassic (Induan) stromatolites and oolites of the Bernburg Formation revisited–microfacies and palaeoenvironment of lacustrine carbonates in Central Germany. *Facies* **67**, 1-31 (2021).
88. A. J. Newell, V. P. Tverdokhlebov, M. J. Benton, Interplay of tectonics and climate on a transverse fluvial system, Upper Permian, Southern Uralian Foreland Basin, Russia. *Sedimentary Geology* **127**, 11-29 (1999).
89. A. J. Newell *et al.*, Disruption of playa–lacustrine depositional systems at the Permo-Triassic boundary: evidence from Vyazniki and Gorokhovets on the Russian Platform. *Journal of the Geological Society* **167**, 695-716 (2010).
90. A. J. Newell *et al.*, Calcretes, fluviolacustrine sediments and subsidence patterns in Permo-Triassic salt-walled minibasins of the south Urals, Russia. *Sedimentology* **59**, 1659-1676 (2012).
91. Z. Zhu *et al.*, Altered fluvial patterns in North China indicate rapid climate change linked to the Permian-Triassic mass extinction. *Scientific Reports* **9**, 16818 (2019).
92. Z. Zhu *et al.*, Intensifying aeolian activity following the end-Permian mass extinction: Evidence from the Late Permian–Early Triassic terrestrial sedimentary record of the Ordos Basin, North China. *Sedimentology* **67**, 2691-2720 (2020).
93. C. Davies, M. B. Allen, M. M. Buslov, I. Safonova, Deposition in the Kuznetsk Basin, Siberia: Insights into the Permian–Triassic transition and the Mesozoic evolution of Central Asia. *Palaeogeography, Palaeoclimatology, Palaeoecology* **295**, 307-322 (2010).
94. S. Mishra, N. Aggarwal, N. Jha, Palaeoenvironmental change across the Permian-Triassic boundary inferred from palynomorph assemblages (Godavari Graben, south India). *Palaeobiodiversity and Palaeoenvironments* **98**, 177-204 (2018).
95. R. M. H. Smith, Changing fluvial environments across the Permian-Triassic boundary in the Karoo Basin, South Africa and possible causes of tetrapod extinctions. *Palaeogeography, Palaeoclimatology, Palaeoecology* **117**, 81-104 (1995).
96. M. R. Gibling, R. Jia, R. A. Gastaldo, J. Neveling, H. Rochín-Bañaga, Braided-river architecture of the Triassic Swartberg member, Katberg formation, South Africa: Assessing age, fluvial style, and paleoclimate after the end-Permian extinction. *Journal of Sedimentary Research* **93**, 741-775 (2023).
97. J. Botha *et al.*, New geochemical and palaeontological data from the Permian-Triassic boundary in the South African Karoo Basin test the synchronicity of terrestrial and marine extinctions. *Palaeogeography, Palaeoclimatology, Palaeoecology* **540**, 109467 (2020).
98. M. F. Miller, J. W. Collinson, Trace fossils from Permian and Triassic sandy braided stream deposits, Central Transantarctic Mountains. *Palaios* **9**, 605-610 (1994).
99. C. R. Fielding *et al.*, Sedimentology of the continental end - Permian extinction event in the Sydney Basin, eastern Australia. *Sedimentology* **68**, 30-62 (2021).
100. S. McLoughlin, S. Lindström, A. N. Drinnan, Gondwanan floristic and sedimentological trends during the Permian–Triassic transition: new evidence from the Amery Group, northern Prince Charles Mountains, East Antarctica. *Antarctic Science* **9**, 281-298 (1997).
101. D. C. G. Ravidà, L. Caracciolo, W. A. Heins, H. Stollhofen, Reconstructing environmental signals across the Permian-Triassic boundary in the SE Germanic basin: Paleodrainage modelling and quantification of sediment flux. *Global and Planetary Change* **206**, 103632 (2021).
102. L. Caracciolo *et al.*, Reconstructing environmental signals across the Permian-Triassic boundary in the SE Germanic Basin: A Quantitative Provenance Analysis (QPA) approach. *Global and Planetary Change*, 103631 (2021).

103. Q. Wu *et al.*, The terrestrial end-Permian mass extinction in the paleotropics postdates the marine extinction. *Science Advances* **10**, eadi7284 (2024).
104. P. Nutiprapun *et al.*, Effects of El Niño drought on seedling dynamics in a seasonally dry tropical forest in Northern Thailand. *Global Change Biology* **29**, 451-461 (2023).
105. W. Yang *et al.*, Paleoenvironmental and paleoclimatic evolution and cyclo- and chrono-stratigraphy of upper Permian–Lower Triassic fluvial-lacustrine deposits in Bogda Mountains, NW China — Implications for diachronous plant evolution across the Permian–Triassic boundary. *Earth-Science Reviews* **222**, 103741 (2021).
106. V. P. Tverdokhlebov, G. I. Tverdokhlebova, A. V. Minikh, M. V. Surkov, M. J. Benton, Upper Permian vertebrates and their sedimentological context in the South Urals, Russia. *Earth-Science Reviews* **69**, 27-77 (2005).
107. T. Kearsey, R. J. Twitchett, A. J. Newell, The origin and significance of pedogenic dolomite from the Upper Permian of the South Urals of Russia. *Geological Magazine* **149**, 291-307 (2012).
108. G. K. Taylor *et al.*, Magnetostratigraphy of Permian/Triassic boundary sequences in the Cis-Urals, Russia: No evidence for a major temporal hiatus. *Earth and Planetary Science Letters* **281**, 36-47 (2009).
109. F. Scholze *et al.*, A multistratigraphic approach to pinpoint the Permian-Triassic boundary in continental deposits: The Zechstein–Lower Buntsandstein transition in Germany. *Global and Planetary Change* **152**, 129-151 (2017).
110. J. W. Schneider, R. Rössler, R. Werneburg, F. Scholze, S. Voigt, paper presented at the CPC-2014 Field Meeting on Carboniferous and Permian Nonmarine–Marine Correlation, Freiberg, Germany, 2014.
111. M. J. Benton, A. J. Newell, Impacts of global warming on Permo-Triassic terrestrial ecosystems. *Gondwana Research* **25**, 1308-1337 (2014).
112. S. Bourquin *et al.*, The Permian–Triassic transition and the onset of Mesozoic sedimentation at the northwestern peri-Tethyan domain scale: Palaeogeographic maps and geodynamic implications. *Palaeogeography, Palaeoclimatology, Palaeoecology* **299**, 265-280 (2011).
113. J. Bodnar, E. P. Coturel, J. I. Falco, M. Beltrán, An updated scenario for the end-Permian crisis and the recovery of Triassic land flora in Argentina. *Historical Biology* **33**, 3654-3672 (2021).
114. G. Cornamusini *et al.*, A lithostratigraphic reappraisal of a Permian-Triassic fluvial succession at Allan Hills (Antarctica) and implications for the terrestrial end-Permian extinction event. *Palaeogeography, Palaeoclimatology, Palaeoecology* **627**, 111741 (2023).
115. S. G. Thomas *et al.*, Palaeosol stratigraphy across the Permian–Triassic boundary, Bogda Mountains, NW China: Implications for palaeoenvironmental transition through earth's largest mass extinction. *Palaeogeography, Palaeoclimatology, Palaeoecology* **308**, 41-64 (2011).
116. A. Bercovici, Y. Cui, M.-B. Forel, J. Yu, V. Vajda, Terrestrial paleoenvironment characterization across the Permian–Triassic boundary in South China. *Journal of Asian Earth Sciences* **98**, 225-246 (2015).
117. J. H. Powell *et al.*, The Permian -Triassic Boundary, Dead Sea, Jordan: Transitional alluvial to marine depositional sequences and biostratigraphy. *Rivista Italiana di Paleontologia e Stratigrafia* **122**, 23-40 (2016).
118. N. Benaouiss, A. Tourani, S. Bourquin, N.-E. Jalil, Late Permian to early Middle Triassic palaeoenvironmental reconstructions of the High Atlas, Morocco: Geodynamic and climate implications in the intertropical western Peri-Tethyan domain. *Palaeogeography, Palaeoclimatology, Palaeoecology* **630**, 111809 (2023).

119. A. Wilson, S. Flint, T. Payenberg, E. Tohver, L. Lanci, Architectural styles and sedimentology of the fluvial Lower Beaufort Group, Karoo Basin, South Africa. *Journal of Sedimentary Research* **84**, 326-348 (2014).
120. N. J. Tabor *et al.*, Evidence of a continuous continental Permian-Triassic boundary section in western equatorial Pangea, Palo Duro Basin, Northwest Texas, U.S.A. *Frontiers in Earth Science* **9**, 747777 (2022).
121. H. S. Jiang *et al.*, Restudy of conodont zonation and evolution across the P/T boundary at Meishan section, Changxing, Zhejiang, China. *Global and Planetary Change* **55**, 39-55 (2007).

Acknowledgements
Mike Orchard is thanked for providing conodont specimens from Idaho. Johann Müller and Nussaïbah Raja helped with the Bayesian age model and generalized additive models. Vladimir V. Silantiev, Fedor A. Mouraviev, Daoliang Chu and Wenchao Shu helped in the field.

Funding:

National Natural Science Foundation of China grants 41821001, 42272022 (YDS)

Deutsche Forschungsgemeinschaft Research Unit TERSANE FOR 2332: Temperature-related stressors as a unifying principle in ancient extinctions; Project Jo 219/15 (MMJ)

Natural Environment Research Council NE/J01799X/1, NE/V001639/1 (DPGB)

Author contributions:

Conceptualization: YDS, AF

Methodology: MMJ, PJV

Investigation: YDS, AF, MMJ, PBW, LK, DPGB, DCGR

Visualization: YDS, AF, DCGR

Funding acquisition: YDS, AF, MMJ, DPGB

Supervision: MMJ, PJV

Writing – original draft: YDS

Writing – review & editing: PBW, AF, MMJ, DPGB, LK

Competing interests: Authors declare that they have no competing interests.

Data and materials availability: All data are available in the main text or the supplementary materials.

Supplementary Materials

Materials and Methods

Supplementary text

Figs. S1 to S18

Tables S1 to S5

References (*56–121*)

Figure captions

Fig. 1 Evolution of the low latitude zonal SST gradient and summary of marine and terrestrial changes across the Permian-Triassic transition. (**A**) Modelled annual mean SSTs of the Changhsingian oceans with 857 ppm pCO_2 forcing. The black rectangle highlights the Niño 3.4 equivalent region for diagnosing ENSO signals. Study sites: Meishan and Laren (China), Vigil (Italy), Mućˊ (Croatia), Georgetown (USA), Kuh-e-Ali Bashi (Iran) and Chanakhchi (Armenia). (**B**) A sharp decrease in the zonal SST gradient across the Tethys from the late Permian to the Early Triassic. The solid black line represents the Locfit analysis of zonal SST gradient data (time window 0.2 Myr, alpha =0.4), with dashed lines bracketing the ±95% confidence interval. Due to uncertainties in paleogeographic reconstruction and sampling sites availability, the zonal SST gradient in equatorial Tethys was primarily calculated from sections between latitudes of 0.5° S and 10° N. (**C**) Carbon isotopes, Tethyan zonal SST gradient, and marine and terrestrial changes across the P-T transition. Siberian Traps eruptions, U-Pb radiometric ages, Hg peak and carbon isotopes (solid blue circles and open diamonds) from the Meishan stratotype section are from (*1, 48, 50-52*). Purple arrows indicate modelled SSTs reproduced in model simulations with 412, 857, 1712, 2568, and 4000 ppm pCO_2 (*53*). The high-resolution Tethyan zonal SST gradient was generated using a generalized additive model (*18*). Charcoal number, macroplant species in equatorial peatlands and correlations between marine and terrestrial P-T records are from (*11, 54*). The last occurrences of Permian reefs, radiolarian species and the chert gaps are from (*43, 44, 46, 55*). Our simulations suggest that MOC (meridional overturning circulation) collapsed as pCO_2 doubled from 412 to 857 ppm. Ocean anoxia developed both in the deep ocean and epicontinental seas.

Fig. 2 Walker circulation (m/s) from each simulation through the Permian-Triassic transition. Positive values indicate descending movements and negative values indicate ascending movements. The Walker circulation weakened during the P-T transition, whilst both ascending and descending limbs contracted towards central Panthalassa.

Fig. 3 Equatorial SST anomalies. Data were calculated from 120 °W to 170 °W longitude and 5 °S to 5 °N latitude (derived from EOF analysis, where EOF1 explains >50% of variance), showing that the intensity and longevity of El Niño-Southern Oscillation increase with atmospheric pCO_2. Red-shaded and blue-shaded areas represent positive and negative anomalies, respectively. Extremely high pCO_2 levels were not required to produce a >3 °C temperature anomaly (the red dashed line highlights the 4 °C anomaly).

Fig. 4 Composite analysis of five consecutive El Niños. Annual mean 1.5 m air temperature (**A-F**) and annual mean precipitation (**G-L**) anomalies during El Niño years, relative to the 100-year climate mean for each time period and pCO_2, in the pre-industrial world and the transition from the pre-crisis (412 ppm) to the peak (4000 ppm) of the P-T crisis world. Our simulations suggest a strong ocean-land teleconnection in low latitudes, with southern high latitudes also being vulnerable to El Niño impacts.

Fig. 5 The compound effect of elevated climate variability and mean state warming showing the rate of change in the Permian-Triassic transition. (**A**) Short-term sea surface temperature variability (dashed line) that is typically controlled by ENSO events. (**B**) A scenario of ~3.5 °C mean state warming over 5 kyr, occurring twice at 251.99 Ma and 251.93 Ma. (**C**) The

compounding effect. If the thermal tolerance of a hypothetical species is 31 °C (T_{max}), increased climate variability accelerates extinction compared to predictions based solely on mean state temperature increases.

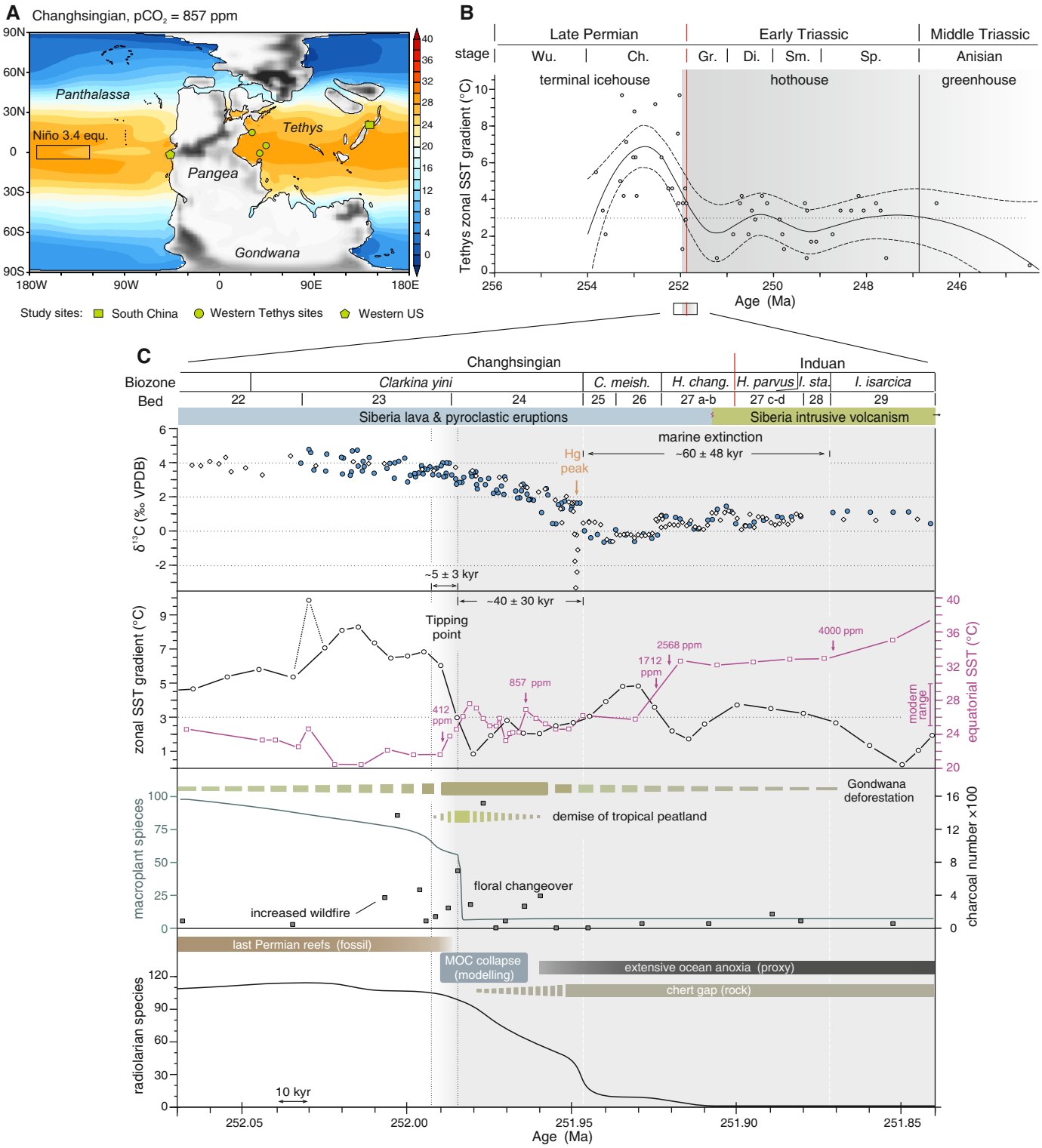
A
Changhsingian, pCO2 = 857 ppm
Panthalassa
Tethys
Pangea
Gondwana
Niño 3.4 equ.
90N
60N
30N
0
30S
60S
90S
180W
90W
0
90E
180E
40
36
32
28
24
20
16
12
8
4
0
Study sites: South China Western Tethys sites Western US
B
Late Permian
Early Triassic
Middle Triassic
stage
Wu.
Ch.
Gr.
Di.
Sm.
Sp.
Anisian
terminal icehouse
hothouse
greenhouse
Tethys zonal SST gradient (°C)
Age (Ma)
C
Changhsingian
Induan
Biozone
Clarkina yini
C. meish.
H. chang.
H. parvus
I. sta.
I. isarcica
Bed
22
23
24
25
26
27 a-b
27 c-d
28
29
Siberia lava & pyroclastic eruptions
Siberia intrusive volcanism
δ13C (‰ VPDB)
marine extinction
Hg peak
~60 ± 48 kyr
~5 ± 3 kyr
~40 ± 30 kyr
zonal SST gradient (°C)
Tipping point
412 ppm
857 ppm
1712 ppm
2568 ppm
4000 ppm
modern range
equatorial SST (°C)
macroplant spieces
Gondwana deforestation
demise of tropical peatland
floral changeover
increased wildfire
charcoal number x100
last Permian reefs (fossil)
MOC collapse (modelling)
extensive ocean anoxia (proxy)
chert gap (rock)
radiolarian species
10 kyr
252.05
252.00
251.95
251.90
251.85
Age (Ma)

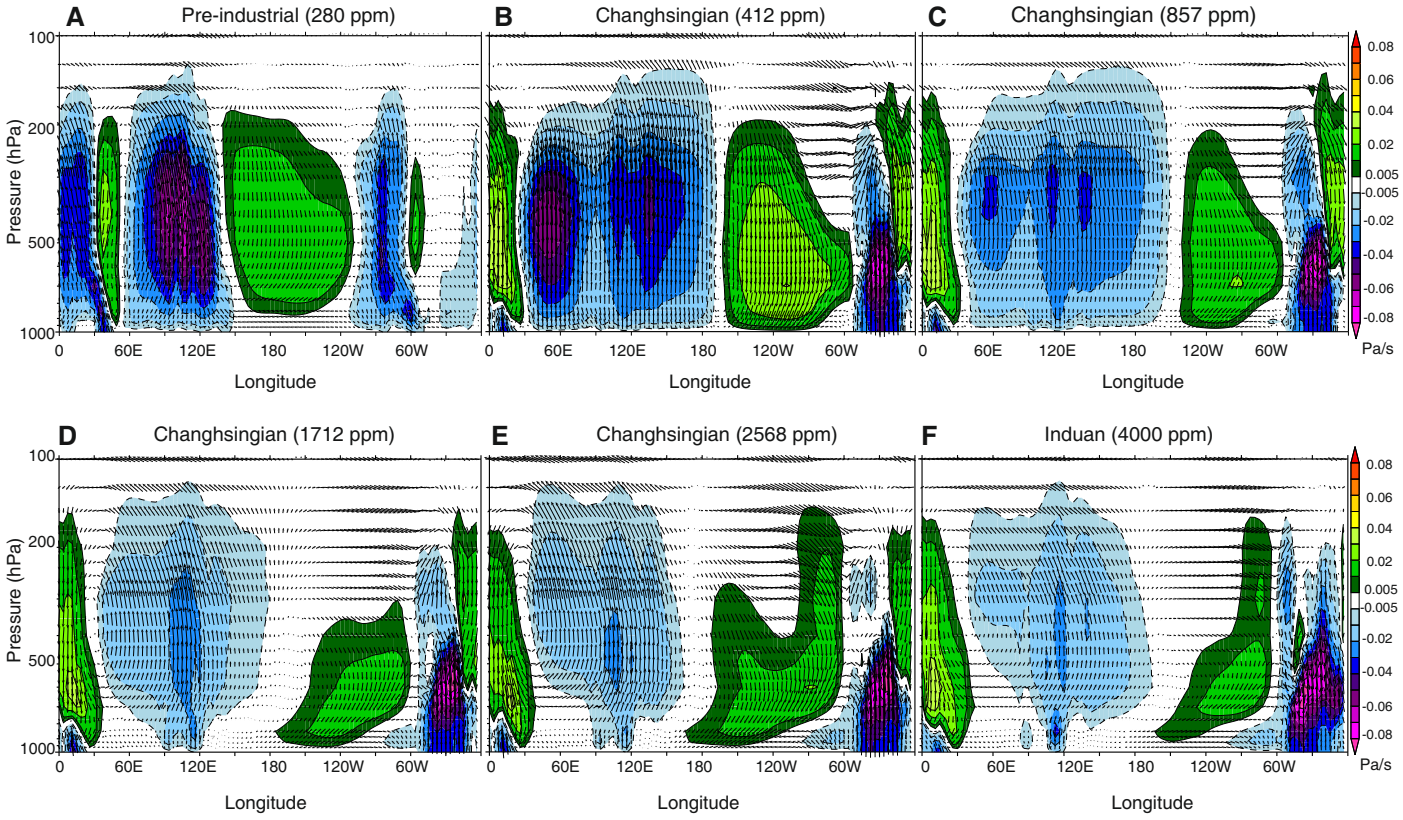
A
Pre-industrial (280 ppm)
B
Changhsingian (412 ppm)
C
Changhsingian (857 ppm)
D
Changhsingian (1712 ppm)
E
Changhsingian (2568 ppm)
F
Induan (4000 ppm)
Pressure (hPa)
100
200
500
1000
0
60E
120E
180
120W
60W
Longitude
0.08
0.06
0.04
0.02
0.005
-0.005
-0.02
-0.04
-0.06
-0.08
Pa/s

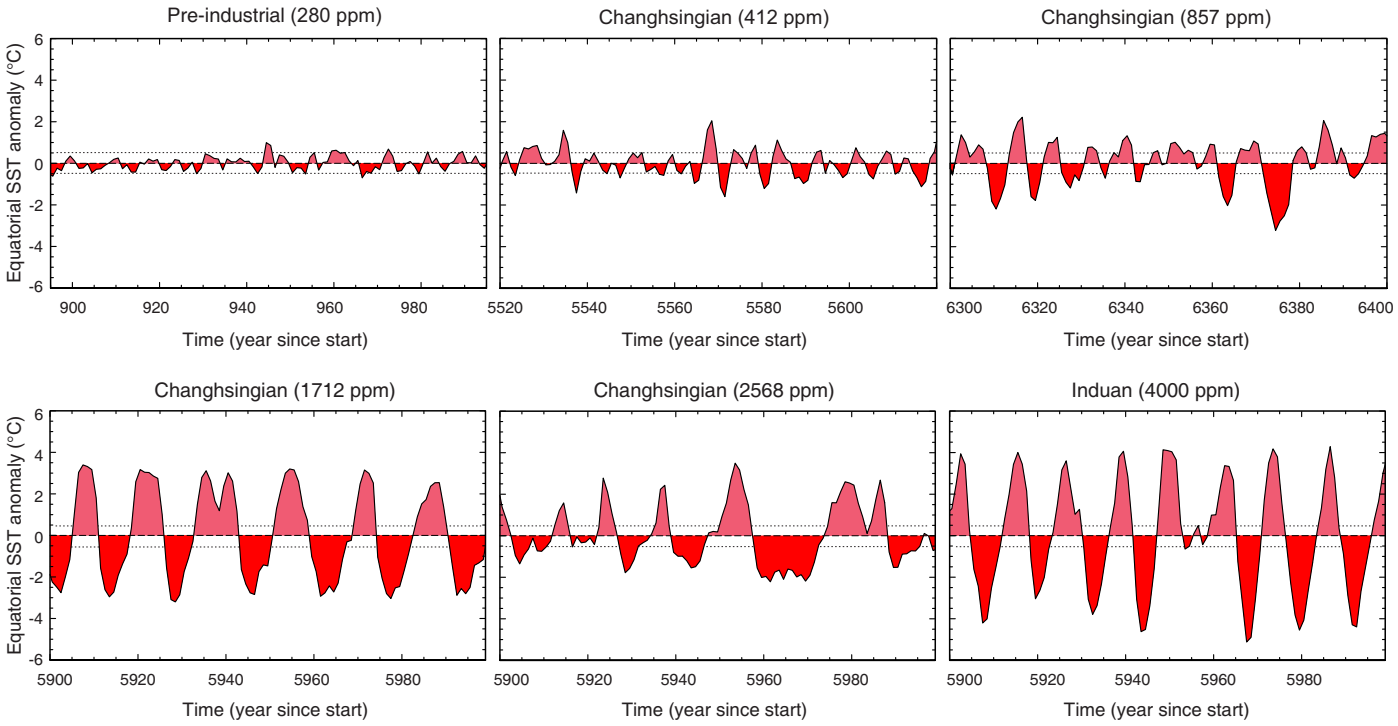
Pre-industrial (280 ppm)
Changhsingian (412 ppm)
Changhsingian (857 ppm)
Changhsingian (1712 ppm)
Changhsingian (2568 ppm)
Induan (4000 ppm)
Equatorial SST anomaly (°C)
6
4
2
0
-2
-4
-6
900
920
940
960
980
5520
5540
5560
5580
5600
6300
6320
6340
6360
6380
6400
5900
5920
5940
5960
5980
Time (year since start)

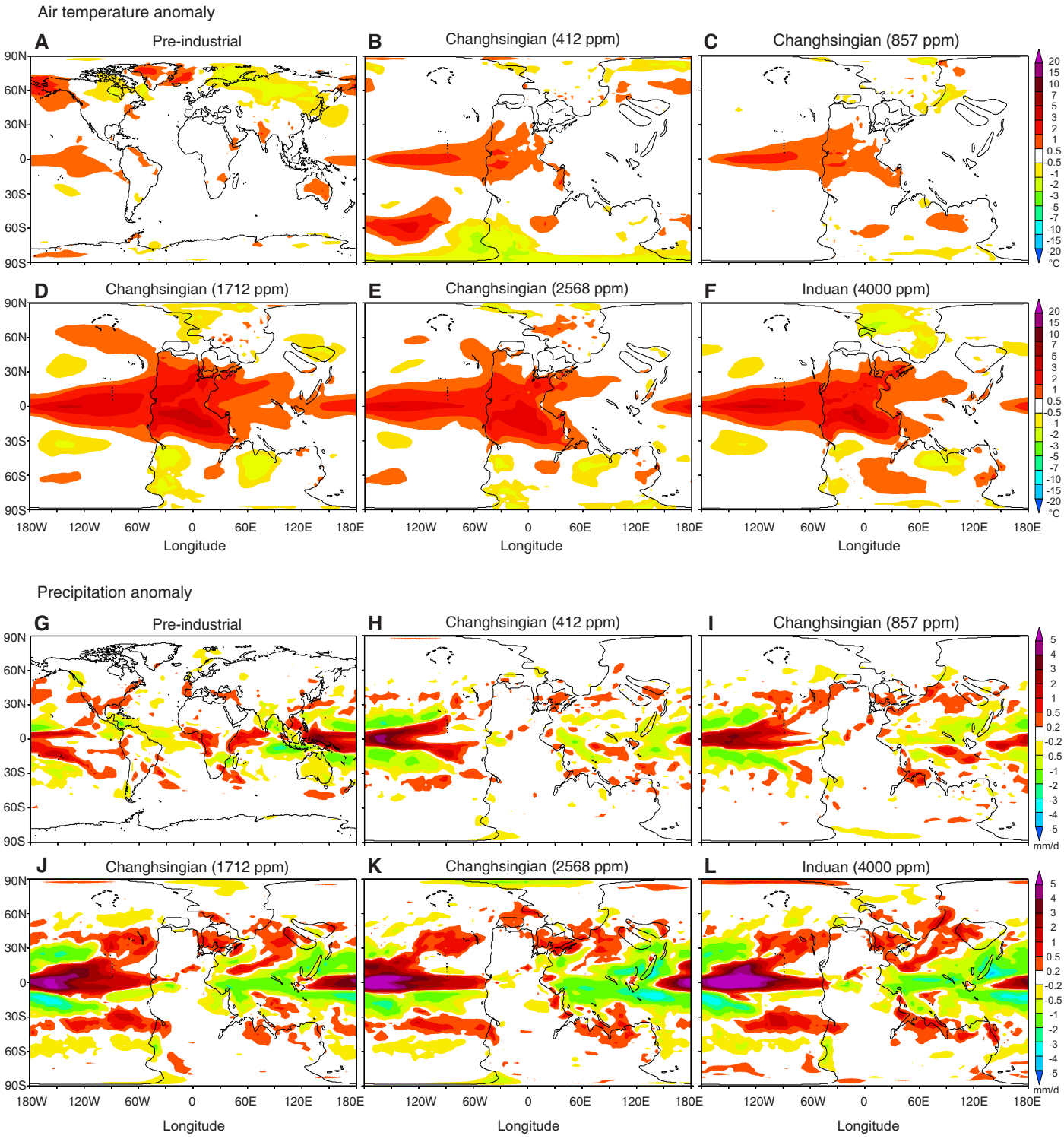
Air temperature anomaly
A
Pre-industrial
B
Changhsingian (412 ppm)
C
Changhsingian (857 ppm)
D
Changhsingian (1712 ppm)
E
Changhsingian (2568 ppm)
F
Induan (4000 ppm)
90N
60N
30N
0
30S
60S
90S
180W
120W
60W
0
60E
120E
180E
Longitude
20
15
10
7
5
3
2
1
0.5
-0.5
-1
-2
-3
-5
-7
-10
-15
-20
°C
Precipitation anomaly
G
Pre-industrial
H
Changhsingian (412 ppm)
I
Changhsingian (857 ppm)
J
Changhsingian (1712 ppm)
K
Changhsingian (2568 ppm)
L
Induan (4000 ppm)
5
4
3
2
1
0.5
0.2
-0.2
-0.5
-1
-2
-3
-4
-5
mm/d

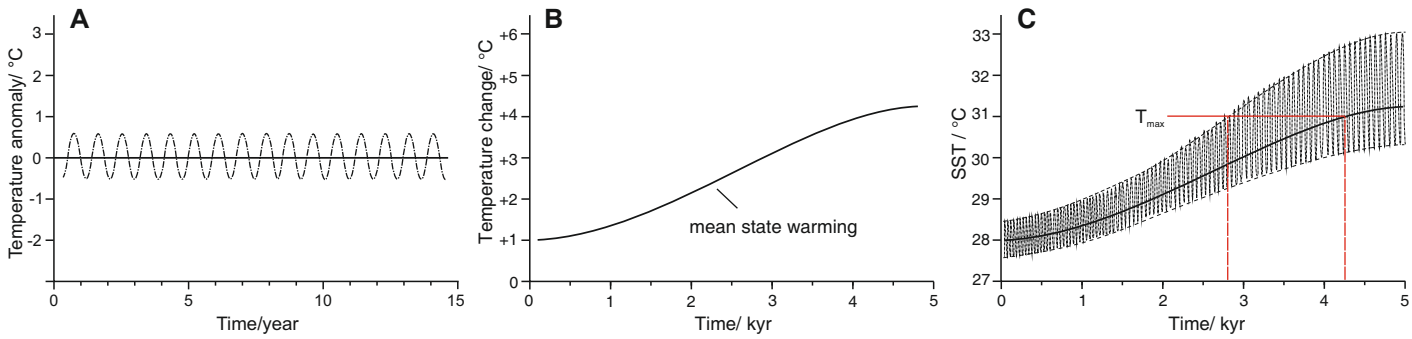
A
Temperature anomaly/ °C
3
2
1
0
-1
-2
0
5
10
15
Time/year
B
Temperature change/ °C
+6
+5
+4
+3
+2
+1
0
0
1
2
3
4
5
Time/ kyr
mean state warming
C
SST / °C
33
32
31
30
29
28
27
0
1
2
3
4
5
Time/ kyr
T max